J⁄M PAPERS

On pressure fluctuations in the near-wall region of turbulent flows

Sergio Pirozzoli[1] and **Tie Wei**[2]

[1]Dipartimento di Ingegneria Meccanica e Aerospaziale, Sapienza Università di Roma, Via Eudossiana 18, 00184 Roma, Italy

[2]Department of Mechanical Engineering, New Mexico Institute of Mining and Technology, 801 Leroy Place, Socorro, NM 87801, USA

Corresponding author: Sergio Pirozzoli, sergio.pirozzoli@uniroma1.it

We study the near-wall behaviour of pressure spectra and associated variances in canonical wall-bounded flows, with a special focus on pipe flow. Analysis of the pressure spectra reveals the universality of small and large scales, supporting the establishment of k^{-1} spectral layers as predicted by fundamental physical theories. However, this universality does not extend to the velocity spectra (Pirozzoli, *J. Fluid Mech.*, vol. 989, 2024, A5), which show a lack of universality at the large-scale end and systematic deviations from the k^{-1} behaviour. We attribute this fundamental difference to the limited influence of direct viscous effects on pressure, with implied large differences in the near-wall behaviour. Consequently, the inner-scaled pressure variances continue to increase logarithmically with the friction Reynolds number as we also infer from a refined version of the attached-eddy model, while the growth of the velocity variance tends to saturate. Extrapolated distributions of the pressure variance at extremely high Reynolds numbers are inferred.

Key words: pipe flow, turbulence simulation, turbulence theory

1. Introduction

Pressure fluctuations in wall-bounded turbulence have been widely investigated due to their important role in structural vibration and acoustic radiation (Blake 2017). Fundamental theoretical predictions regarding the behaviour of pressure fluctuations in boundary layers were made by Bradshaw (1967), who argued that near solid walls but outside the viscous sublayer, the only important length scale is y (normal distance from the wall), the only important velocity scale is $u_\tau = (\tau_w/\rho)^{1/2}$ (friction velocity) and

the pressure scale is τ_w (wall shear stress). Hence, dimensional analysis requires that $E_p(k) = \tau_w^2 y f(ky)$, where E_p is the wavenumber spectral density of pressure fluctuations and k is the wavenumber in any wall-parallel direction. Further assuming universality of the spectrum at the lowest wavenumbers, associated with the largest eddies of the flow, yields $f(ky) \sim 1/(ky)$, hence it follows that $E_p(k) \sim \tau_w^2 k^{-1}$. Leveraging on Townsend's assumption that the near-wall region may be affected from 'wall-attached' eddies of large size which contribute to the Reynolds stress much farther from the wall than the point of observation, but not at the point of observation (Townsend 1961), Bradshaw further realised that the near-wall pressure spectrum can receive contributions at small wavenumbers also from distant eddies. Hence, integration of the k^{-1} energy spectrum over an increasing range of scales results in logarithmic increase of the near-wall pressure variance with the friction Reynolds number at any fixed y^+ location. Logarithmic increase of the pressure variance also results from inner/outer layer overlap arguments applied to pressure fluctuations (Panton *et al.* 2017), and it is the expected behaviour from the attached-eddy model (AEM) (Jiménez & Hoyas 2008; Xu *et al.* 2020).

Experiments have indeed confirmed that the intensity of wall pressure fluctuations expressed in terms of pressure variance in boundary layers and channels tends to increase with the Reynolds number, when scaled by the wall shear stress (e.g. Willmarth 1975; Farabee & Casarella 1991). However, the scatter in experimental measurements is significant. The primary challenge arises from the limited size of transducers, which restricts the resolution of high-frequency components that become increasingly important at high Reynolds numbers. Direct numerical simulations (DNS) (Hu *et al.* 2006; Tsuji *et al.* 2007; Jiménez & Hoyas 2008; Sillero *et al.* 2013; Mehrez *et al.* 2019) have generally confirmed the validity of theoretical inferences regarding logarithmic growth of the pressure variance; however, only partial evidence exists about the existence of an $E_p \sim k^{-1}$ spectral range (Panton *et al.* 2017). This is most likely due to inherent limitations of DNS in achieving high enough Reynolds numbers. In fact, Chen & Sreenivasan (2022) advocated an alternative scenario whereby the growth of wall pressure variance would saturate at infinite Reynolds numbers on account of an assumed bound on the wall dissipation rate of the streamwise velocity variance. Specifically, the wall pressure variance would follow a defect power law, and strict wall scaling would be recovered in the limit of extreme Reynolds numbers.

The goal of the present paper is to get deeper insight into the proper behaviour of pressure fluctuations in the near-wall region of turbulent wall layers in the asymptotically high-Reynolds-number limit, also by contrasting their behaviour with that of the streamwise velocity fluctuations. For that purpose, and similar to what was done by Pirozzoli (2024) for the velocity fluctuations, we first analyse the behaviour of the spectral densities of pressure in the near-wall region, and then extrapolate the high-Reynolds-number behaviour of the pressure variance from integration of the spectral densities.

2. The direct numerical simulation database

The analysis relies on DNS data of fully developed turbulent flow in a circular pipe. Friction Reynolds numbers up to $Re_\tau \approx 12\,000$ are considered (Pirozzoli 2024), which is the current upper limit for DNS. Here, $Re_\tau = R u_\tau / \nu$, with R the pipe radius, u_τ the friction velocity and ρ the fluid density. Inner normalisation by u_τ and $\delta_v = \nu/u_\tau$ is hereafter denoted with a + superscript. Uppercase letters are used to denote mean values of the flow variables and lowercase letters to denote fluctuations thereof. The numerical method is described in detail by Verzicco & Orlandi (1996) and Orlandi (2000), and relies on an implementation of the fractional step method on a staggered cylindrical mesh, whereby uniform

Flow case	L_x/R	Mesh ($N_\theta \times N_r \times N_x$)	Re_b	f	Re_τ	T/τ_t	Line style
B	15	$768 \times 96 \times 768$	17 000	0.02719	495.6	192.9	———
C	15	$1792 \times 164 \times 1792$	44 000	0.02119	1132.2	50.4	———
C-L	30	$1792 \times 164 \times 3584$	44 000	0.02119	1132.3	52.8	·····
C-LL	45	$1792 \times 164 \times 5376$	44 000	0.02114	1131.0	45.3	– –
D	15	$3072 \times 243 \times 3072$	82 500	0.01828	1972.0	45.1	———
E	15	$4608 \times 327 \times 4608$	133 000	0.01657	3026.8	26.9	———
F	15	$9216 \times 546 \times 9216$	285 000	0.01421	6006.4	18.2	———
G	15	$18\,432 \times 1024 \times 18\,432$	612 000	0.01242	12 054.5	6.99	———

Table 1. Flow parameters for DNS of pipe flow. Here R is the pipe radius, L_x is the pipe axial length, N_θ, N_r and N_x are the number of grid points in the azimuthal, radial and axial directions, respectively, $Re_b = 2u_b R/\nu$ is the bulk Reynolds number, $f = 8\tau_w/(\rho u_b^2)$ is the friction factor, $Re_\tau = u_\tau R/\nu$ is the friction Reynolds number, T is the time interval used to collect the flow statistics and $\tau_t = R/u_\tau$ is the eddy turnover time. Cases C-L and C-LL were run to test the sensitivity of the results to the axial pipe length.

volumetric forcing is applied to the axial momentum equation to maintain constant mass flow rate in time. According to this method, pressure is obtained from discrete enforcement of the divergence-free constraint to the velocity field, which results in the solution of a discrete Poisson equation, as explained in detail by Kim & Moin (1985). Furthermore, since pressure is defined at the cell centres and the velocity components are defined at the cell faces, no numerical boundary condition for pressure is required, and pressure is automatically consistent with the discretised form of the momentum equation. This avoids uncertainties and ambiguities in the enforcement of proper boundary conditions for the pressure Poisson equation, which have been extensively discussed (e.g. Gresho & Sani 1987).

A list of the flow cases is reported in table 1, which includes basic information about the computational mesh and some key parameters. As can be seen in table 1, the largest DNS has run for less than 10 eddy turnover times, which is the commonly accepted limit to guarantee time convergence (Hoyas & Jiménez 2006). Nevertheless, careful examination of the time convergence according to the method of Russo & Luchini (2017) has shown that the estimated standard deviation in the prediction of the pressure and velocity variances in the range of wall distances under scrutiny here is at most 0.6 %. Power spectral densities of velocity and pressure are hereafter reported, which we obtained by taking Fourier transform in the azimuthal direction, and averaging in the axial direction and in time. The associated uncertainties are expected to be larger than for the basic flow statistics; however, the confidence bands shown in figure 5 convey that errors in the velocity spectra are mainly confined to the largest wavelengths, and they are barely visible in the pressure spectra. Details of the sensitivity of the flow statistics to the pipe length are provided in Appendix A.

3. Pressure spectra and the attached-eddy model

To start with, we compare the spectra of streamwise velocity and pressure to highlight similarities and differences. Figure 1(*a*) shows the spectral density of the streamwise velocity (E_u), as a function of the wall distance (y) and of the spanwise wavelength (λ_θ), pre-multiplied by $k_\theta = 2\pi/\lambda_\theta$, for flow case G. The figure highlights the presence of a prominent energetic buffer-layer peak scaling in wall units, and an outer energetic site showcasing R-sized superstructures previously observed in experiments (Kim & Adrian 1999; Hellström & Smits 2014). Between these two primary locations, a band of energetic intermediate modes is observed, with lengths roughly proportional to their distance from the wall, as after the AEM (see Townsend 1976; Hwang 2015; Marusic & Monty 2019).
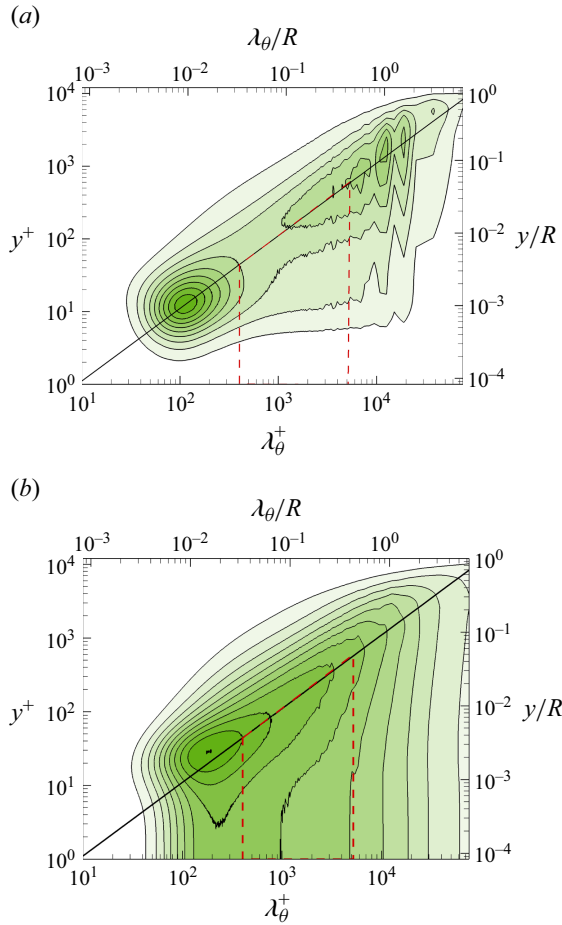
(a)

(b)

Figure 1. Flow case G: pre-multiplied spanwise spectral densities of fluctuating streamwise velocity $k_\theta^+ E_u^+$ (a) and pressure $k_\theta^+ E_p^+$ (b), as a function of wavelength and wall distance. Wall distances and wavelengths are reported both in inner units (bottom, left axes) and in outer units (top, right axes). The diagonal line denotes the trend $y_s^+ = 0.11\lambda_\theta^+$, and the trapezoidal region bounded by the red dashed line marks the region of near-wall influence of attached eddies. Contour levels are shown from 0.36 to 3.6, in intervals of 0.36 in (a) and from 0.3 to 3, in intervals of 0.3 in (b).

In particular, we find that the 'centre' of attached eddies with size λ_θ resides at $y_s \approx 0.11\lambda_\theta$. The separation between the two energetic sites is about two orders of magnitude in flow case G. The figure also clarifies that the influence of the attached eddies and the $O(R)$ eddies on streamwise velocity fluctuations extends down to the wall. Specifically, the spectral iso-lines tend to attain a triangular shape between the spectral ridge and the wall due to energy 'leakage' from the overlying eddies. This region influenced by wall-attached eddies is marked with dashed red lines in figure 1, indicating an upper wall distance beyond which the influence of outer eddies is not felt. Setting the boundary between attached eddies and large eddies at $\lambda_\theta = 0.5R$ (past which isolated maxima of the spectral density emerge), it follows that the maximum wall distance where their influence is felt is $y_{max}^+ \approx 0.055 \, Re_\tau$, with $y_{max}^+ \approx 660$ at the highest Reynolds number under scrutiny here. This 'near-wall' region is the main subject of investigation in the present study.

The spectral map for pressure fluctuations is shown for contrast in figure 1(b). The overall structure seems to be similar to that of the streamwise velocity, with a clear inner
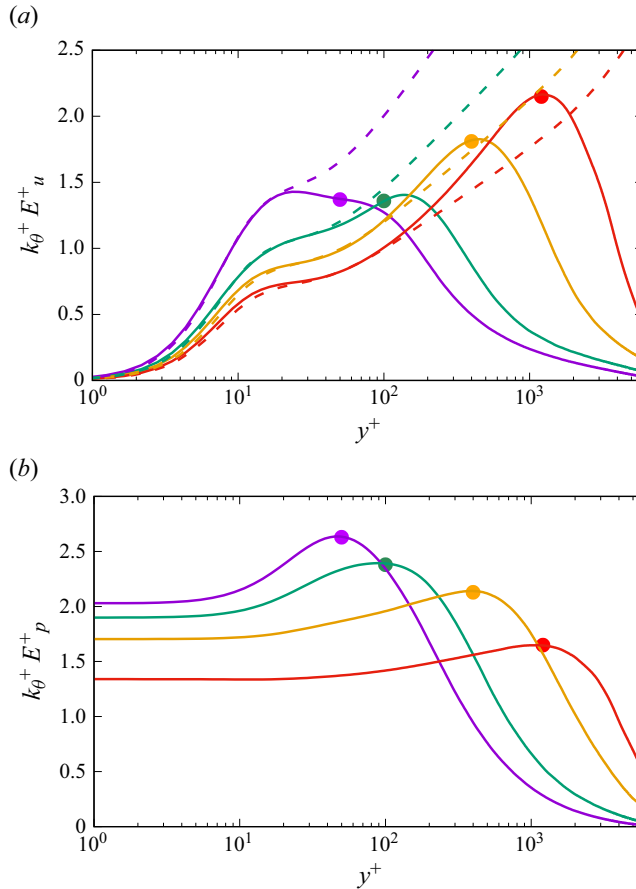
Figure 2. Flow case G: pre-multiplied spectral density of axial velocity (*a*) and pressure (*b*) as a function of wall distance, corresponding to various wavelengths: $\lambda_\theta^+ = 455$ ($y_s^+ = 50$) (purple), $\lambda_\theta^+ = 909$ ($y_s^+ = 100$) (green), $\lambda_\theta^+ = 3636$ ($y_s^+ = 400$) (orange), $\lambda_\theta^+ = 10970$ ($y_s^+ = 1205$) (red). The filled circles denote the wall distance of the corresponding eddy centres (y_s); see figure 1. The dashed lines in (*b*) denote predictions of Bradshaw (1967). The directory including the data and the Jupyter notebook that generated this figure can be accessed at https://www.cambridge.org/S0022112025002642/JFM-Notebooks/files/figure_2.

energetic site centred in the buffer layer, and a diagonal ridge to be interpreted as the signature of wall-attached eddies. Some differences are, however, noteworthy. First, the velocity spectra reveal a distinct outer-layer spectral peak at $\lambda_\theta \approx R$, which is absent in the pressure spectra. This finding suggests that superstructures do not induce significant pressure variations. Second, along the primary spectral ridge (solid line in the figure), the behaviour differs markedly: the spectral density of pressure decreases monotonically, while the velocity spectral density exhibits a dip between the inner and outer energetic regions. Third, and most relevant to this study, the iso-lines of the pressure spectral density tend to extend down to the wall almost orthogonally. This feature is especially striking when comparing with figure 1(*a*), which instead indicates decreasing behaviour as the wall is approached. This essential difference in the near-wall behaviour of velocity and pressure has a large impact on the flow statistics, as discussed in the following.

In order to more clearly bring out this aspect, in figure 2 we show wall-normal profiles of $k_\theta^+ E_u^+$ and $k_\theta^+ E_p^+$ for various values of λ_θ in the range of wavelengths between the inner and the outer energetic sites. In the AEM interpretation, these characterise the variance of
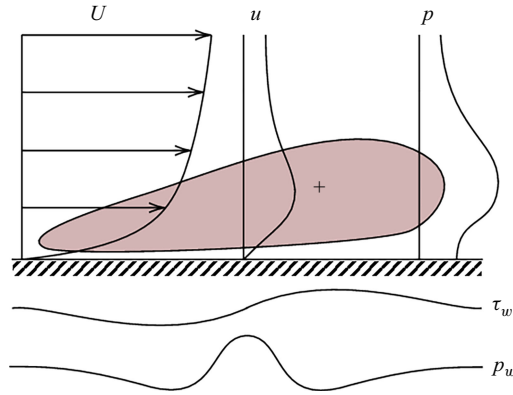
Figure 3. Illustrative sketch of velocity and pressure perturbations associated with a wall-attached eddy (u, p), along with corresponding wall signatures (τ_w, p_w). The cross identifies the tentative eddy centre.

streamwise velocity and pressure fluctuations induced by attached eddies with size λ_θ and centred along the main spectral ridge of figure 1. As shown by Pirozzoli (2024), the wall-normal profiles of E_u very well conform with the theoretically predicted distributions of the velocity variance resulting from 'turbulent Stokes layers', which are shown with dashed lines. Indeed, according to Bradshaw (1967), the effect of 'distant' wall-attached eddies on the near-wall region is mainly a low-frequency modulation of the wall shear stress, to which turbulence has time to readjust, in such a way that the law-of-the-wall applies instantaneously. This simple scheme offers a compelling explanation for why the spectral density of streamwise velocity is influenced by the wall even well above the viscous sublayer. In contrast, the spectral densities of pressure extend down to the wall almost orthogonally, with little attenuation relative to the peak value observed at the centre of the corresponding attached eddies.

A conceptual sketch illustrating these observations is provided in figure 3. The main idea is that a wall-attached eddy produces both velocity and pressure fluctuations. However, due to differing boundary conditions, it leaves a direct pressure imprint at the wall, while its velocity influence primarily manifests as a change in local wall shear stress. We note that the wall signatures shown in the figure are indicative only, as they depend on the specifics of the particular AEM (see e.g. Ahn *et al.* 2010). The AEM (Townsend 1976; Marusic & Monty 2019) can be used to make predictions of the velocity and pressure statistics, under the critical assumptions that (*a*) the attached eddies are self-similar and (*b*) the eddies are not cross-correlated. Assuming for simplicity flow over a flat wall at $y = 0$, the velocity perturbation at point $\mathbf{x} = (x, y, z)$ from one representative eddy of height h, rooted at $\mathbf{x}_e = (x_e, 0, z_e)$, and with a characteristic velocity scale u_o is given by

$$u_i(\mathbf{x}) = u_o f_i \left(\frac{\mathbf{x} - \mathbf{x}_e}{h} \right), \tag{3.1}$$

where $u_1 = u$, $u_2 = v$ and $u_3 = w$ refer to the streamwise, wall-normal and spanwise components of fluctuating velocity. Adding up the contributions of wall-attached eddies of various heights, one then obtains the distribution of the Reynolds stresses:

$$\langle u_i u_j \rangle (y) = u_o^2 \int_{\delta_1}^{\delta} P(h) I_{ij} (y/h) \, \mathrm{d}h, \tag{3.2}$$

where $P(h)$ is the probability distribution function of eddies of a given height;

$$I_{ij}(\eta) = \int_{-\infty}^{\infty} \int_{-\infty}^{\infty} f_i(\xi, \eta, \zeta) f_j(\xi, \eta, \zeta) \, \mathrm{d}\xi \, \mathrm{d}\zeta, \tag{3.3}$$

with $\xi = x/h$, $\eta = y/h$, $\zeta = z/h$, is the contribution from an individual eddy to the velocity correlations; and δ_1 and δ are the smallest and largest eddy length scales, respectively. Townsend (1976) reasoned that, on account of the no-penetration condition at the wall, f_1 and f_3 are asymptotically finite for $\eta \to 0$, whereas $f_2 \sim \eta$. This leads to the requirements that for small η,

$$I_{12} \simeq A_{12}\eta, \quad I_{11} \simeq A_{11}, \quad I_{22} \simeq A_{22}\eta^2, \quad I_{33} \simeq A_{33}, \tag{3.4}$$

with A_{12}, A_{11}, A_{22}, A_{33} non-zero constants. Townsend then deduced the distribution of eddy sizes with wall distance necessary to produce invariance of the inner-scaled Reynolds shear stress $(-\langle uv \rangle/u_\tau^2 \approx 1)$ with distance from the wall, as nominally observed in the logarithmic layer. This analysis leads to setting $u_o = u_\tau$ and having $P(h) \sim 1/h$. With this, it follows that the other components of the Reynolds stress tensor must have the form

$$\langle u^2 \rangle/u_\tau^2 = B_1 - A_1 \log(y/\delta), \tag{3.5}$$

$$\langle v^2 \rangle/u_\tau^2 = B_2, \tag{3.6}$$

$$\langle w^2 \rangle/u_\tau^2 = B_3 - A_2 \log(y/\delta). \tag{3.7}$$

We extend the AEM to pressure fluctuations by considering the Poisson equation that they satisfy, as given by (Kim 1989)

$$\frac{1}{\rho} \frac{\partial^2 p}{\partial x_j \partial x_j} = -2 \frac{\mathrm{d}U}{\mathrm{d}y} \frac{\partial v}{\partial x} - \frac{\partial u_i}{\partial x_j} \frac{\partial u_j}{\partial x_i}, \tag{3.8}$$

where $x_1 = x$, $x_2 = y$ and $x_3 = z$. The appropriate wall boundary condition for pressure is derived from enforcing momentum balance in the wall-normal direction, resulting in

$$\frac{1}{\rho} \left. \frac{\partial p}{\partial y} \right|_{y=0} = \nu \left. \frac{\partial^2 v}{\partial y^2} \right|_{y=0}. \tag{3.9}$$

Additional background and details of the pressure Poisson equation for turbulent wall-bounded flows can be found in Appendix B. Assuming a similarity solution for pressure fluctuations of the form

$$p(x, y, z) = \rho u_\tau^2 f_p(\xi, \eta, \zeta), \tag{3.10}$$

and noting that in the logarithmic layer $\mathrm{d}U/\mathrm{d}y = u_\tau/\kappa y$, (3.8) can be approximated with

$$\frac{\partial^2 f_p}{\partial \xi_j \partial \xi_j} = -\frac{2}{\kappa \eta} \frac{\partial f_2}{\partial \xi} - \frac{\partial f_i}{\partial \xi_j} \frac{\partial f_j}{\partial \xi_i}. \tag{3.11}$$

As for the boundary condition (3.9), in terms of similarity variables it becomes

$$\left. \frac{\partial f_p}{\partial \eta} \right|_{\eta=0} = \frac{1}{h^+} \left. \frac{\partial^2 f_2}{\partial \eta^2} \right|_{\eta=0}, \tag{3.12}$$

with $h^+ = hu_\tau/\nu$ the typical shear Reynolds number for a given attached eddy. For eddies whose centre is sufficiently distant from the wall, to which the AEM is supposed to apply, $h^+ \gg 1$, and hence the previous boundary condition becomes
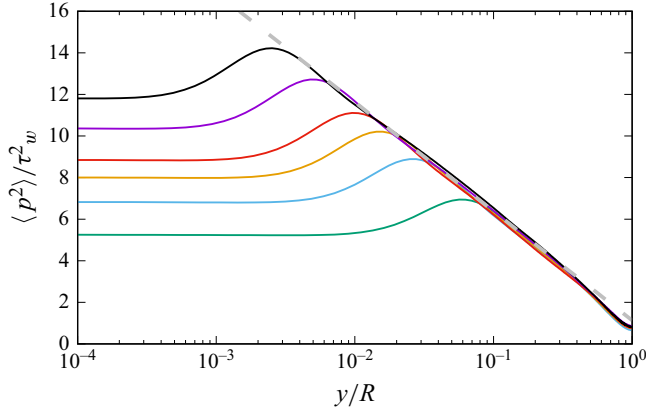
Figure 4. Distribution of pressure variance as a function of outer-scaled wall distance. The colour codes correspond to different Reynolds numbers, as defined in table 1. The dashed grey line indicates the prediction of (3.17), with $B_p = 1.13$, $C_p = 2.28$. The directory including the data and the Jupyter notebook that generated this figure can be accessed at https://www.cambridge.org/S0022112025002642/JFM-Notebooks/files/figure_4.

$$\left. \frac{\partial f_p}{\partial \eta} \right|_{\eta=0} = 0. \tag{3.13}$$

Equations (3.11) and (3.13) show that wall-attached similarity solutions for the pressure field are possible if the velocity field is self-similar. This is a key result which allows one to extend Townsend's formalism to pressure in straightforward manner, yielding

$$\langle p^2 \rangle(y) = \tau_w^2 \int_{\delta_1}^{\delta} P(h) I_p(\eta) \mathrm{d}h, \tag{3.14}$$

with

$$I_p(\eta) = \int_{-\infty}^{\infty} \int_{-\infty}^{\infty} f_p^2(\xi, \eta, \zeta) \mathrm{d}\xi \, \mathrm{d}\zeta. \tag{3.15}$$

The approximate boundary condition (3.13) implies that f_p at the wall is finite and independent of h, whence it follows that, for small η,

$$I_p \simeq A_p, \tag{3.16}$$

with A_p a non-zero constant, which figure 2(*b*) well supports. Substitution into (3.14) and carrying out the integral as suggested by Perry & Chong (1982, Appendix B) yields

$$\langle p^2 \rangle / \tau_w^2 = B_p - C_p \log(y/\delta). \tag{3.17}$$

The prediction of (3.17) is very well verified in the pipe flow DNS data, with constants $B_p = 1.13$, $C_p = 2.28$ (Yu *et al.* 2022). Indeed, figure 4 shows the presence of an extremely long logarithmic layer ranging from the buffer layer all the way up to $y/R \approx 0.5$. This evidence is far more convincing than that supporting the existence of a logarithmic layer for $\langle u^2 \rangle$, which is relatively thin and still debated (e.g. Monkewitz 2022). We interpret this as a result of near-wall viscous effects on velocity, which undermine the inviscid asymptotic predictions of (3.4). Therefore, we propose that (3.17) is the most robust prediction derived from the AEM.
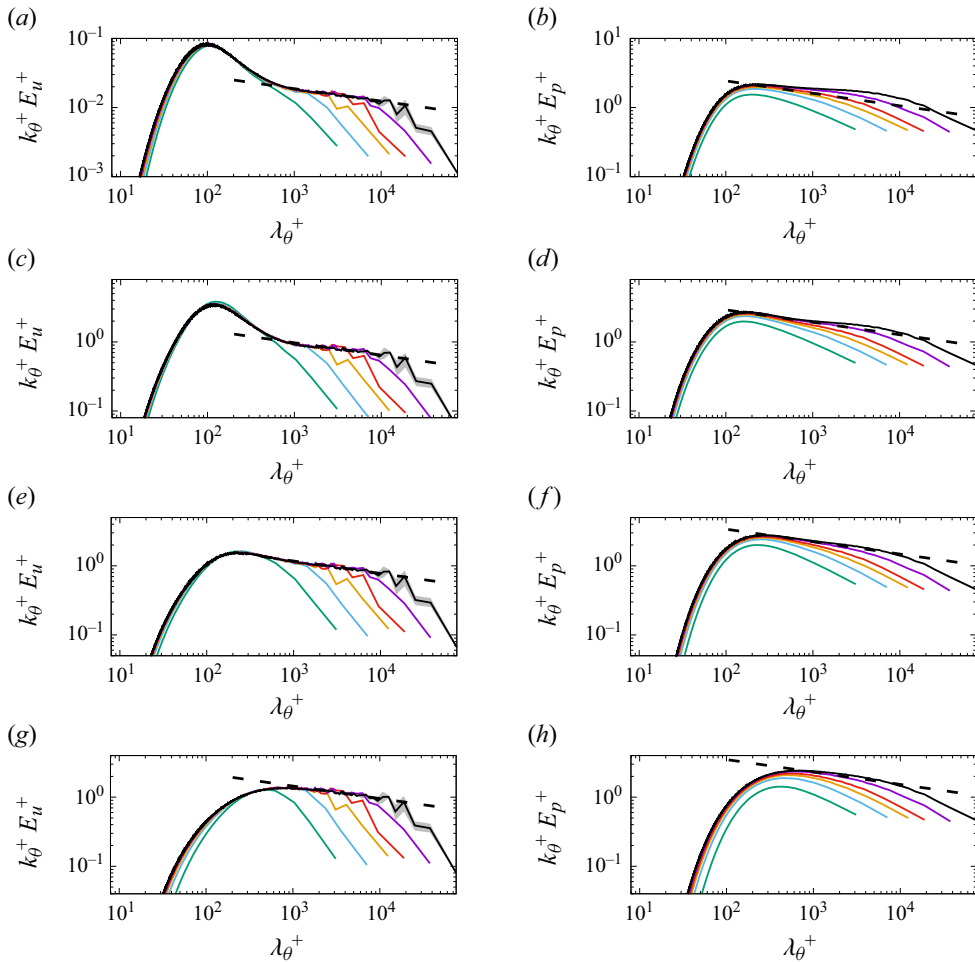
1010 A10-8

Figure 5. For caption see next page.

4. Analysis of the spectra

The arguments presented in § 1 for the pressure fluctuation spectra by Bradshaw (1967), which lead to the $E_p \sim \tau_w^2 k^{-1}$ spectrum, can similarly be applied to velocity fluctuations, resulting in the prediction $E_u \sim u_\tau^2 k^{-1}$. This is the key contribution of the work of Perry & Abell (1977). In figure 5, we present the spanwise spectral densities of streamwise velocity and pressure fluctuations at various locations with fixed $y^+ < y_{max}^+$. Uncertainty bars for flow case G are shown in grey, illustrating that the effects of limited time convergence on the velocity spectra are mainly concentrated at scales $\lambda_\theta \gtrsim R$. Time convergence of the pressure spectra appears to be very nearly perfect. The figure provides clear evidence for the tendency towards universality at the small-scale end of the spectra when inner normalisation is applied. However, this tendency manifests more rapidly for the velocity field ($Re_\tau \gtrsim 2000$) than for the pressure field, which appears to attain universal behaviour only at the highest Reynolds number examined. In the velocity field, the universal inner layer extends towards larger scales. In contrast, the large-scale end of the pressure spectra still seems far from achieving a universal behaviour. The general trend for the pressure field is an increase in spectral density, potentially forming a plateau at the highest
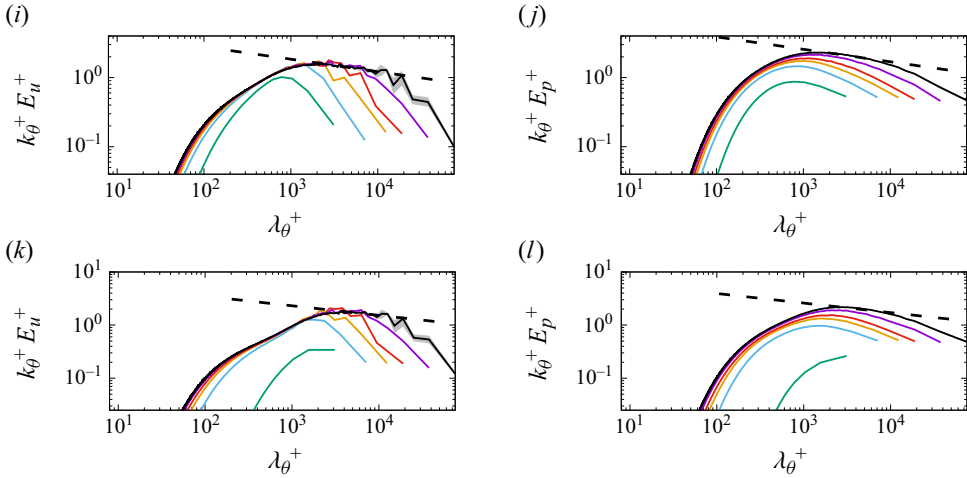
Figure 5 *(cntd)*. Pre-multiplied spanwise spectral densities of streamwise velocity (*a,c,e,g,i,k*) (from Pirozzoli 2024) and pressure (*b,d,f,h,j,l*) in inner scaling, at various inner-scaled wall distances: $y^+ = 1$ (*a,b*), $y^+ = 15$ (*c,d*), $y^+ = 50$ (*e,f*), $y^+ = 100$ (*g,h*), $y^+ = 200$ (*i,j*), $y^+ = 400$ (*k,l*). The colour codes indicate different Reynolds numbers as given in table 1. The shaded grey regions denote the expected range of uncertainty for flow case G. The dashed black lines denote the $\lambda_\theta^{+-0.18}$ trend. The directory including the data and the Jupyter notebook that generated this figure can be accessed at https://www.cambridge.org/S0022112025002642/JFM-Notebooks/files/figure_5.

Reynolds numbers. This observation aligns with Panton *et al.* (2017), who inferred a similar behaviour from channel flow data, suggesting a k^{-1} spectral range.

Spectral overlap arguments as those used by Bradshaw (1967) and Perry & Abell (1977) were used by Pirozzoli (2024) to infer the plausible behaviour of the velocity spectra, which can also be applied to the pressure spectra. By assuming that: (i) the typical velocity of all eddies is the friction velocity and (ii) the typical length of the smaller eddies is δ_v, whereas the typical length of the larger eddies is R, it follows that the spectral signature of the smaller eddies can be expressed as

$$k_\theta^+ E^+ = f(\lambda_\theta^+), \tag{4.1}$$

while the larger eddies are expected to follow a spectrum of the form

$$k_\theta^+ E^+ = g(\lambda_\theta / R). \tag{4.2}$$

Assuming an overlap spectral layer exists between these inner- and outer-scaled regions, the functions f and g should take the form of either power laws or logarithmic functions. Based on the DNS data, the power-law description appears to be more appropriate. Hence, the spectral densities in the overlap layer are expected to behave as

$$k_\theta^+ E^+ = C\left(\lambda_\theta^+\right)^{-\alpha} = CRe_\tau^{-\alpha}\left(\frac{\lambda_\theta}{R}\right)^{-\alpha}, \tag{4.3}$$

holding in inner and outer scaling, respectively, where α and C could in general depend on y^+. Equation (4.3) includes the k_θ^{-1} spectral scaling as a special case, occurring for $\alpha = 0$. In that case, both the small-scale and the large-scale ends of the spectrum would be universal.

Figure 5 indeed supports the validity of (4.3) for the streamwise velocity, suggesting the occurrence of an overlap layer with power-law scaling with exponent $\alpha \approx 0.18$, as we have estimated by fitting the DNS data for flow case G in the range of wavelengths
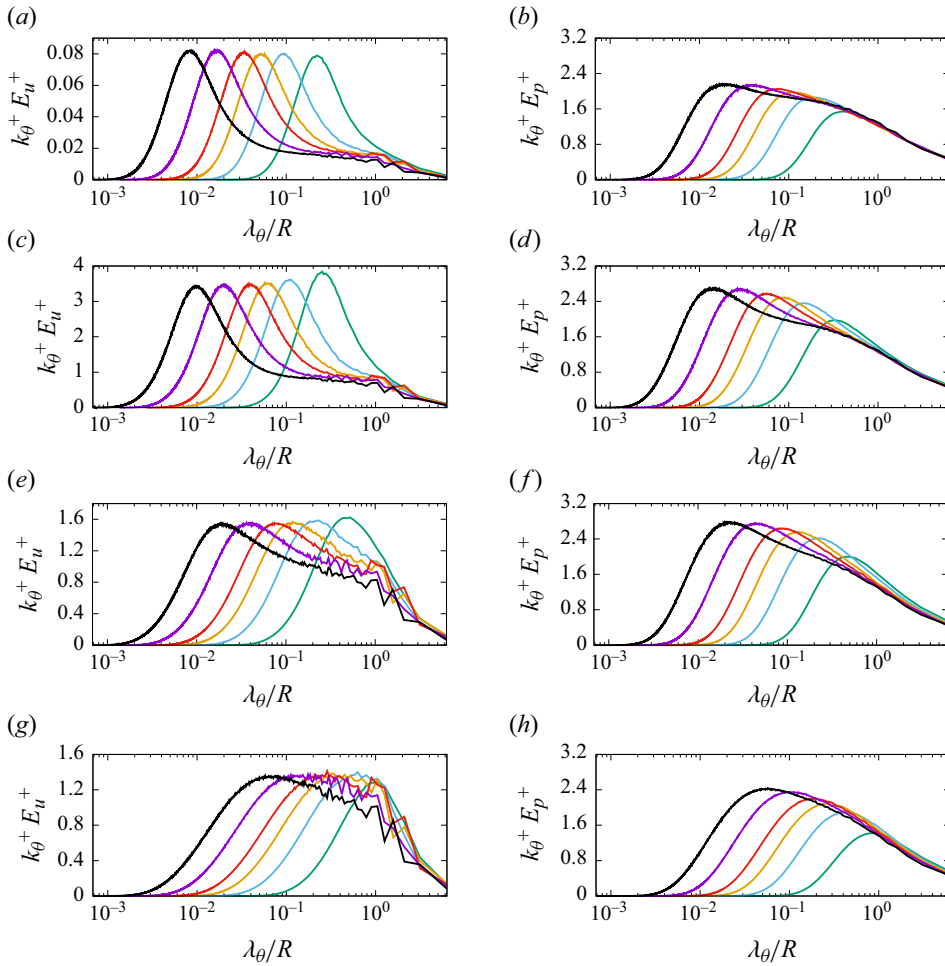
Figure 6. For caption see next page.

$1000 \leqslant \lambda_\theta^+ \leqslant 10\,000$ (Pirozzoli 2024). Notably, we confirm that the spectral power-law exponent remains universal with respect to changes in wall distance and Reynolds number, and, within numerical uncertainty, is consistent even in channel flow (Pirozzoli 2024). The behaviour of pressure spectra is not so clear-cut, although the decay exponent is certainly less than for the streamwise velocity, and energy pile-up is still visible as the Reynolds number increases, reflecting imperfect universality of the small scales of motion.

In figure 6, the spectral densities of velocity and pressure are shown as a function of the outer-scaled wavelength. The universality of the velocity spectra is clearly not as pronounced as seen for the small wavelengths in figure 5. The energy associated with the large scales of motion becomes slightly but consistently less at higher Reynolds numbers for a given λ_θ/R. Inspection of (4.3) shows that this behaviour is consistent with the occurrence of a negative power law in the intermediate scales. On the other hand, the large-scale end of the pressure spectra appears to be very nearly independent of both the Reynolds number and of the wall distance, given that the corresponding iso-lines of the spectral map in figure 1(*b*) are vertically straight. Based on the theoretical prediction (4.3), the universality at the large scales and the tendency towards (though imperfect)
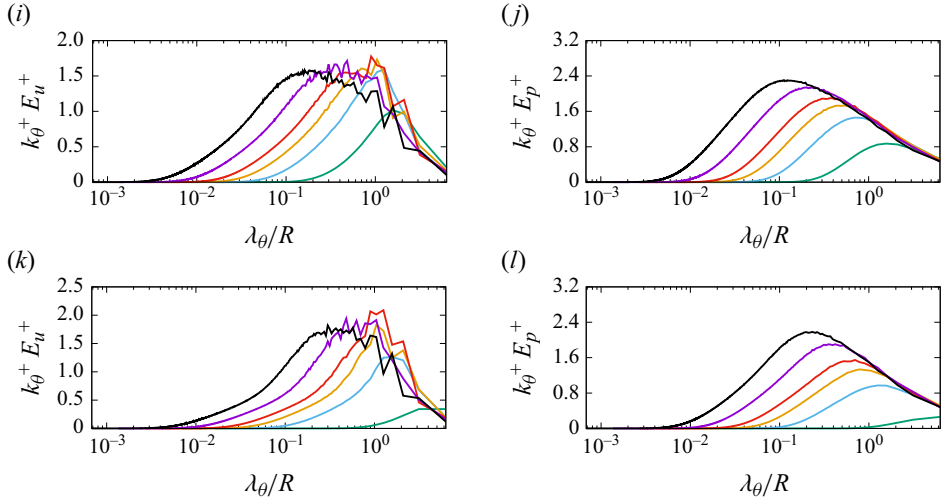
Figure 6 *(cntd).* Pre-multiplied spanwise spectral densities of streamwise velocity (*a,c,e,g,i,k*) (from Pirozzoli 2024) and pressure (*b,d,f,h,j,l*) in outer scaling, at various inner-scaled wall distances: $y^+ = 1$ (*a,b*), $y^+ = 15$ (*c,d*), $y^+ = 50$ (*e,f*), $y^+ = 100$ (*g,h*), $y^+ = 200$ (*i,j*), $y^+ = 400$ (*k,l*). The colour codes indicate different Reynolds numbers as given in table 1. The directory including the data and the Jupyter notebook that generated this figure can be accessed at https://www.cambridge.org/S0022112025002642/JFM-Notebooks/files/figure_6.

universality at the small scales, the only asymptotically possible behaviour for pressure is a k^{-1} spectrum, as predicted by Bradshaw (1967).

For completeness, in figure 7 we also report the spectral densities of velocity and pressure as a function of the outer-scaled wavelength at fixed values of y/R, to highlight scaling in the outer part of the wall layer. At these wall distances the contamination from viscous effects is minimal, and universality across Reynolds-number variation is effectively achieved. However, whereas some scatter at the largest scales remains in the velocity spectra, the pressure spectra are very nearly universal. This is in our opinion a very important result as it speaks about tendency for the near-wall flow to achieve universality in viscous units, but also for the flow in the pipe core to become universal when expressed in R units, in support of the scenario envisaged by Dennis & Sogaro (2014). Universality of the large scales in the near-wall region is retained in the pressure spectra, but it is lost in the velocity spectra on account of viscous effects, recalling the discussion of figure 2.

5. The pressure variance

The information derived from the analysis of the velocity and pressure spectra can be distilled to infer the behaviour of the velocity and pressure variances, taking inspiration from Hwang (2024). Let λ_s and λ_ℓ be, respectively, indicative lower and upper limits for the observed overlap spectral range. The velocity variance can be expressed as

$$\langle u^2 \rangle^+ = \underbrace{\int_{-\infty}^{\log \lambda_s^+} k_\theta^+ E_u^+ \mathrm{d} \log \lambda_\theta^+}_{\langle u^2 \rangle_s^+} + \underbrace{\int_{\log \lambda_s^+}^{\log \lambda_\ell^+} k_\theta^+ E_u^+ \mathrm{d} \log \lambda_\theta^+}_{\langle u^2 \rangle_o^+} + \underbrace{\int_{\log \lambda_\ell^+}^{\infty} k_\theta^+ E_u^+ \mathrm{d} \log \lambda_\theta^+}_{\langle u^2 \rangle_\ell^+},$$
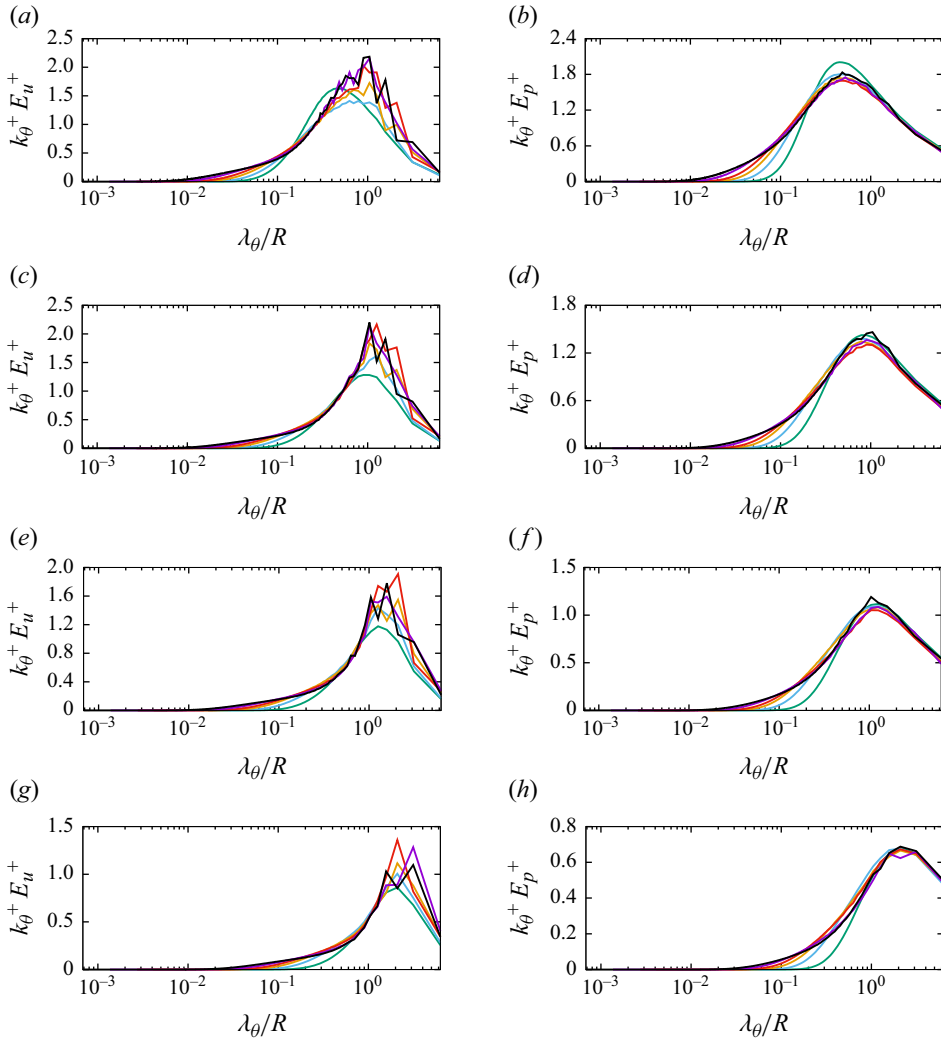
(5.1)

Figure 7. Pre-multiplied spanwise spectral densities of streamwise velocity (*a,c,e,g*) (from Pirozzoli 2024) and pressure (*b,d,f,h*) in outer scaling, at various outer-scaled wall distances: $y/R = 0.1$ (*a,b*), $y/R = 0.2$ (*c,d*), $y/R = 0.3$ (*e,f*), $y/R = 0.5$ (*g,h*). The colour codes indicate different Reynolds numbers as given in table 1. The directory including the data and the Jupyter notebook that generated this figure can be accessed at https://www.cambridge.org/S0022112025002642/JFM-Notebooks/files/figure_7.

where the subscripts s, ℓ and o denote, respectively, the contributions of the smallest scales, the largest scales and the intermediate, overlap-layer scales. Likewise, the pressure variance can be expressed as

$$\langle p^2 \rangle^+ = \underbrace{\int_{-\infty}^{\log \lambda_s^+} k_\theta^+ E_p^+ \mathrm{d} \log \lambda_\theta^+}_{\langle p^2 \rangle_s^+} + \underbrace{\int_{\log \lambda_s^+}^{\log \lambda_\ell^+} k_\theta^+ E_p^+ \mathrm{d} \log \lambda_\theta^+}_{\langle p^2 \rangle_o^+} + \underbrace{\int_{\log \lambda_\ell^+}^{\infty} k_\theta^+ E_p^+ \mathrm{d} \log \lambda_\theta^+}_{\langle p^2 \rangle_\ell^+} .$$

(5.2)

Although the precise values of the limits in (5.1) are not important, it is crucial that the lower limit scales in wall units, hence $\lambda_s^+ = \text{const.}$, and that the upper limit scales in outer

units, hence $\lambda_\ell/R = $ const. Based on the previous analysis of the velocity spectra, Pirozzoli (2024) showed that the behaviour of the velocity variance should be as follows:

$$\langle u^2 \rangle^+ = A_u(y^+) - B_u(y^+)Re_\tau^{-\alpha}, \tag{5.3}$$

with A_u and B_u functions of the wall distance to be determined by fitting the DNS data.

Based on evidence previously given that the pressure spectra at the small and large scales tend to be universal across the Re_τ range, the associated contribution to the pressure variance is expected to be asymptotically constant, and hence

$$\langle p^2 \rangle_s^+ = A_s(y^+), \quad \langle p^2 \rangle_\ell^+ = A_\ell(y/R) \approx \text{const}. \tag{5.4}$$

Last, the contribution of the overlap layer can be evaluated by integrating the power-law spectrum given in (4.3) corresponding to $\alpha = 0$, thus obtaining

$$\langle p^2 \rangle_o^+ = A_o(y^+) + B_o(y^+) \, \log Re_\tau. \tag{5.5}$$

Combining the previous equations, it follows that overall pressure variance should vary as

$$\langle p^2 \rangle^+ = A_p(y^+) + B_p(y^+) \, \log Re_\tau, \tag{5.6}$$

where the functions A_p and B_p do not depend explicitly on the Reynolds number, given the assumptions made to define λ_s and λ_ℓ. This formula predicts that, at any fixed y^+, the pressure variance should increase logarithmically with Re_τ, in agreement with the arguments of Bradshaw (1967) and Perry & Abell (1977), and with the predictions of the AEM presented in § 3. Equation (5.6) is tested in figure 8, where we show the contributions to the pressure variance from small, large and intermediate scales, having set $\lambda_s^+ = 400$, $\lambda_\ell = R/2$. In agreement with the pressure spectra, the contribution from the large scales (figure 8b) is found to be very nearly universal when reported as a function of the outer-scaled coordinate y/R. The contributions from the small scales (figure 8a) show deviations from universality at relatively low Re; however, saturation is close to complete at $Re_\tau = 12\,000$ (black line). The contribution from the intermediate scales is instead found to grow continuously, as after (5.5); see figure 8(c). Comparison of the various contributions for flow case G (figure 8d) shows that all of them tend to assume flat behaviour near the wall, again consistent with the notion that pressure fluctuations are not directly affected by viscosity. The contribution from the small scales (dashed lines) has a peak in the buffer layer, which is reflected in the peak of the overall variance. The contribution from the superstructures (dotted lines) is nearly constant across the wall layer with a peak at $y/R \approx 0.1$, whereas the contribution from the intermediate scales (dot-dashed lines) has a peak at an intermediate distance from the wall, here $y^+ \approx 200$. Values for the asymptotic constants A_p, B_p in (5.6) determined from fitting the DNS data at representative off-wall locations are reported in table 2, along with the corresponding standard deviations.

The resulting distributions of the pressure variances as a function of Re_τ are shown in figure 9, at various y^+ locations. In the figure we contrast the logarithmic fits predicted from (5.6) with the defect power law given in (5.3). For comparison, fits of the streamwise velocity variance are also displayed. As shown by Pirozzoli (2024), velocity variances are clearly better fitted with the defect power law than from the logarithmic law. Whereas the defect power law could well be mistaken for logarithmic growth at $y^+ = 15$, the trends at positions farther from the wall are distinctly different from logarithmic. As for pressure, the logarithmic law (5.6) yields perfect fit of the DNS data, across the entire Reynolds-number range, and at all off-wall stations. Larger scatter is observed when data are fitted with a defect power-law distribution. To provide a quantitative impression, the standard deviation for the logarithmic fit of the pressure variance at
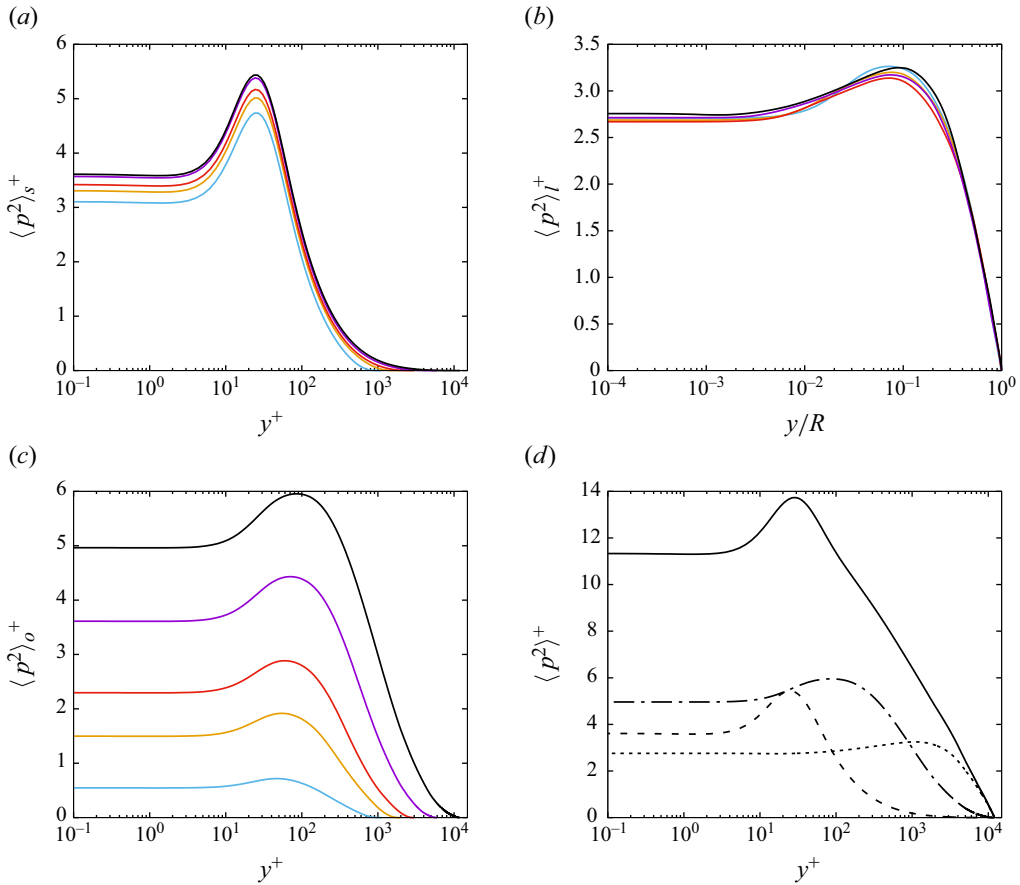
Figure 8. Contributions to pressure variance in pipe flow from: small scales (*a*), large scales (*b*) and intermediate scales (*c*). (*d*) The pressure variance for flow case G ($Re_\tau \approx 12\,000$), and the contributions from small scales (dashed lines), from large scales (dotted lines) and from intermediate scales (dash-dotted lines). The colour codes correspond to different Reynolds numbers, as defined in table 1. The directory including the data and the Jupyter notebook that generated this figure can be accessed at https://www.cambridge.org/S0022112025002642/JFM-Notebooks/files/figure_8.

$y^+ = 50$ is 0.045, whereas the defect power-law fit yields a standard deviation of 0.24. The different behaviour of velocity and pressure is made manifest in figure 9(*e*), where we show the ratio of pressure to streamwise velocity variances. Note that the data are not shown at $y^+ = 1$ as the velocity variance there is very small, so this indicator is off scale. Whereas at low-to-moderate Reynolds number there is no obvious trend, with logarithmic increase at near-wall stations ($y^+ = 15, 50$) and flat behaviour farther from the wall, there is very little ambiguity for $Re_\tau \gtrsim 3000$, at which an increasing logarithmic trend is observed at all y^+, with the same growth rate. In our opinion, this is very convincing evidence that streamwise velocity variance and pressure variance behave in a different way, the streamwise velocity variance tending to saturate with the Reynolds number following a defect power law, and pressure variance following an ever-increasing logarithmic trend.

Figure 10 shows extrapolated distributions of the pressure variance as a function of wall distance for various Re_τ. In addition to confirming that the predictive formula (5.6) accurately represents the range of Reynolds numbers used to inform the model, the figure

Station	$A_p(y^+)$	$B_p(y^+)$
$y^+ = 1$	-7.73 ± 0.207 (2.67 %)	2.08 ± 0.0262 (1.26 %)
$y^+ = 15$	-7.41 ± 0.0929 (1.25 %)	2.23 ± 0.0118 (0.529 %)
$y^+ = 50$	-7.85 ± 0.138 (1.76 %)	2.28 ± 0.0175 (0.768 %)
$y^+ = 100$	-9.64 ± 0.117 (1.22 %)	2.29 ± 0.0148 (0.648 %)
$y^+ = 200$	-11.6 ± 0.131 (1.12 %)	2.35 ± 0.0165 (0.705 %)
$y^+ = 400$	-14.1 ± 0.211 (1.50 %)	2.46 ± 0.0258 (1.09 %)

Table 2. Fitting parameters to use in (5.6), based on DNS data fitting, at several off-wall positions, with accompanying asymptotic standard errors.
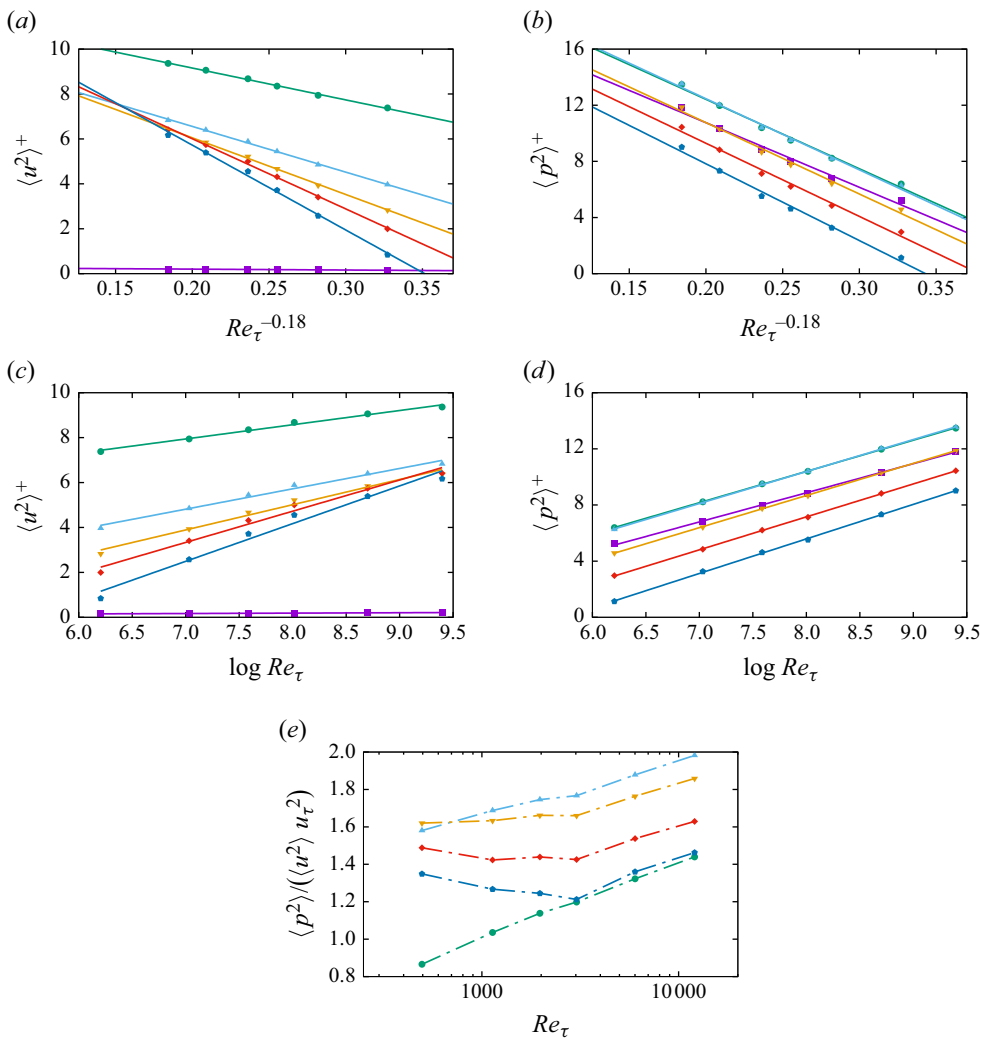

Figure 9. Variances of (*a,c*) streamwise velocity and (*b,d*) pressure, as a function of $Re_\tau^{-0.18}$ (*a,b*) and as a function of $\log Re_\tau$ (*c,d*), at various off-wall positions: $y^+ = 1$ (purple), $y^+ = 15$ (green), $y^+ = 50$ (cyan), $y^+ = 100$ (orange), $y^+ = 200$ (red), $y^+ = 400$ (blue). (*e*) The ratio of pressure to streamwise velocity variances as a function of Re_τ. The directory including the data and the Jupyter notebook that generated this figure can be accessed at https://www.cambridge.org/S0022112025002642/JFM-Notebooks/files/figure_9.
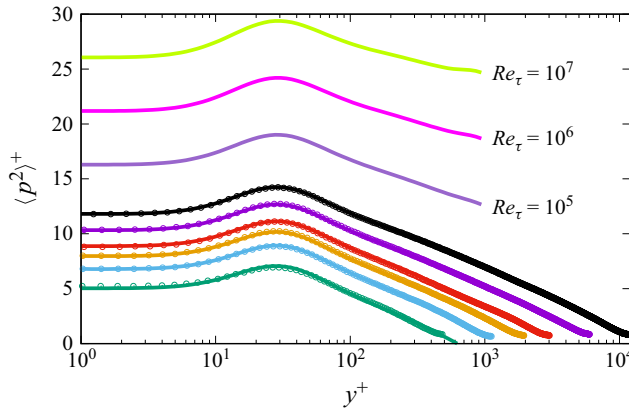
Figure 10. Predicted distributions of pressure variances at various Re_τ, according to (5.6). The symbols denote the DNS data used to determine the fitting coefficients $A_p(y^+)$, $B_p(y^+)$ (see table 1 for the colour codes). The directory including the data and the Jupyter notebook that generated this figure can be accessed at https://www.cambridge.org/S0022112025002642/JFM-Notebooks/files/figure_10.

also illustrates extrapolations beyond this range. Unlike the streamwise velocity variance (Pirozzoli 2024), the growth does not saturate, and the shape of the pressure variance distribution remains consistent. Instead, there is continuous growth, primarily driven by the expanding range of scales associated with wall-attached eddies, as predicted by (5.6).

6. Conclusions

We have studied pressure fluctuations in the near-wall region of turbulent wall layers using pipe flow DNS data. We find that spectral maps are key to properly understanding the phenomenon. Although the structure of the spectral maps of pressure is similar to those of the streamwise velocity field, featuring a clear imprint of wall-attached eddies in the near-wall region, the details differ significantly. Specifically, while the velocity imprint of wall-attached eddies becomes fainter as the wall is approached due to the impeding effect of viscosity, the pressure footprint remains nearly constant, as pressure does not directly feel the effects of viscosity. This results in different spectral behaviours at any fixed wall distance. Whereas the pre-multiplied streamwise velocity spectra tend to slightly decay at large wavelengths, the corresponding pressure spectra exhibit a tendency for a plateau. In this case, the classical k^{-1} spectral scaling envisioned by Bradshaw (1967) emerges, while deviations result in a shallower exponent for the streamwise velocity. This leads to qualitative differences in the behaviour of the corresponding variances, which can be inferred from the integration of the spectral densities. In particular, while the streamwise velocity is predicted to saturate at any fixed y^+ as Re_τ increases, pressure is predicted to undergo sustained logarithmic growth. Although differences between the two trends may be difficult to capture in today's DNS, they lead to vastly different behaviours in the very-high-Re_τ limit.

The results we obtain for pressure are, in a sense, not very surprising, as they align with classical knowledge dating back to the work of Bradshaw (1967). However, this scenario has recently been questioned by Chen & Sreenivasan (2022), who argued that pressure variance should follow a behaviour similar to that of the streamwise velocity variance. We contend that this is not the case. The identified differences in the behaviour of velocity and pressure are somewhat surprising, given that velocity and pressure are related through the pressure Poisson equation (3.8). Hence, it would be reasonable to expect the same scaling
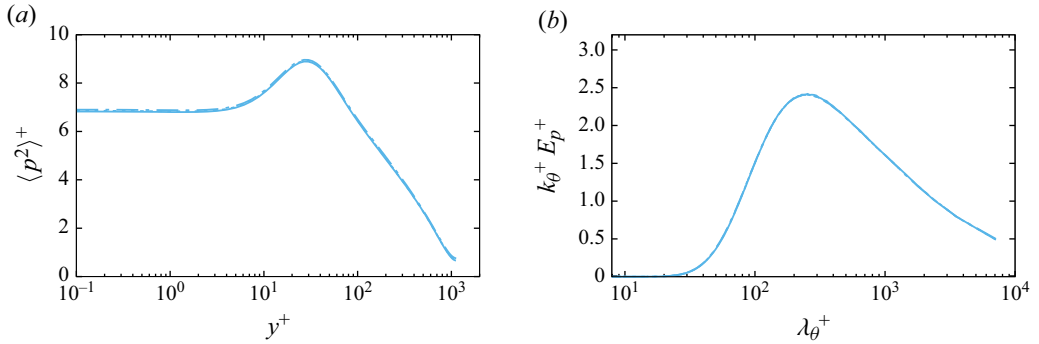
(a)

(b)

Figure 11. Analysis of sensitivity to pipe length for (*a*) pressure variance and (*b*) pre-multiplied spanwise spectral density of pressure at $y^+ = 50$. Flow cases C, C-L and C-LL are shown; see table 1 for line styles.

for the two quantities. However, it is important to note that the pressure Poisson equation explicitly encompasses non-local interactions, particularly the long-range effects of outer-layer large eddies (whose strength certainly scales with u_τ) on the near-wall region, which are not impeded by viscosity. As the Reynolds number increases, an increasing number of wall-attached eddies accumulate for a fixed y^+, and their effects combine to yield logarithmic growth of the pressure variance. In this regard, in § 3, we provide the first proof that wall-attached self-similar solutions for the pressure field are possible if the velocity field is also self-similar, thereby integrating pressure consistently within the AEM.

Appendix A. Pipe length sensitivity analysis

The sensitivity of the computed results to the pipe length assumed in the DNS has been assessed through additional simulations conducted at $Re_b = 44\,000$ (flow case C), as listed in table 1. Specifically, we have doubled and tripled the pipe length in flow cases C-L and C-LL, respectively. These flow cases have been simulated for numerous eddy turnover times, for the purpose of minimising the time sampling error. The resulting change in the distribution of the pressure variance is well below 1 %, as illustrated in figure 11(*a*). Figure 11(*b*) additionally presents a comparison of the pre-multiplied pressure spectra at $y^+ = 50$, again showing that the pipe length has very little influence on the flow properties herein considered and remaining numerical uncertainties primarily stem from finite time sampling.
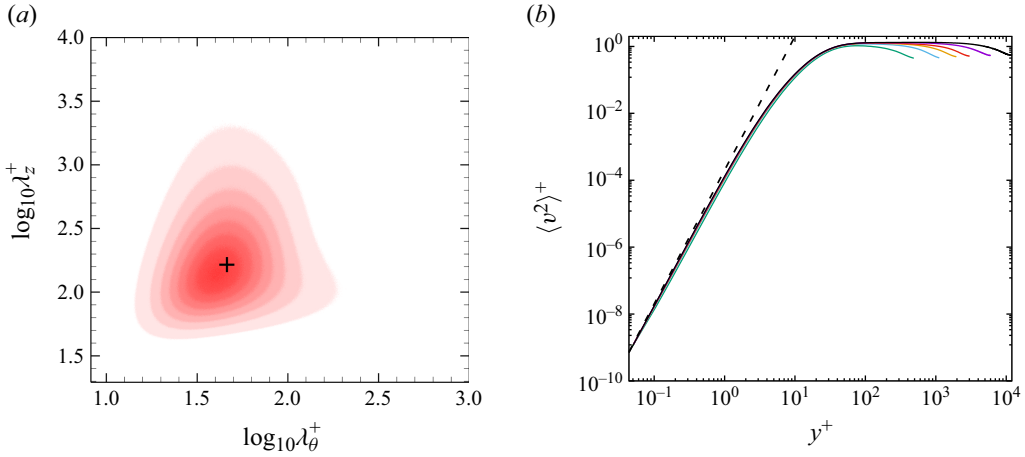
Figure 12. (*a*) Two-dimensional, pre-multiplied spectral density of wall-normal velocity at $y^+ = 1$ for flow case G and (*b*) distribution of wall-normal velocity variance in log–log scale for the flow cases listed in table 1. In (*a*) the cross denotes the peak location, corresponding to $\lambda_\theta^+ \approx 41.1$, $\lambda_z^+ \approx 144.2$. The dashed line in (*b*) denotes the trend $\langle v^2 \rangle^+ = 2 \times 10^{-4} (y^+)^4$.

Appendix B. On the solution of the pressure Poisson equation

Since the problem (3.8) + (3.9) has a linear nature, its general solution can be found from the solution of three subproblems, namely (Mansour *et al.* 1988)

$$\frac{1}{\rho} \frac{\partial^2 p_r}{\partial x_j \partial x_j} = -2 \frac{\mathrm{d}U}{\mathrm{d}y} \frac{\partial v}{\partial x}, \qquad \left. \frac{\partial p_r}{\partial y} \right|_{y=0} = 0, \tag{B1}$$

$$\frac{1}{\rho} \frac{\partial^2 p_s}{\partial x_j \partial x_j} = -\frac{\partial u_i}{\partial x_j} \frac{\partial u_j}{\partial x_i}, \qquad \left. \frac{\partial p_s}{\partial y} \right|_{y=0} = 0, \tag{B2}$$

$$\frac{1}{\rho} \frac{\partial^2 p_{st}}{\partial x_j \partial x_j} = 0, \qquad \left. \frac{1}{\rho} \frac{\partial p_{st}}{\partial y} \right|_{y=0} = \nu \left. \frac{\partial^2 v}{\partial y^2} \right|_{y=0}. \tag{B3}$$

The first part (p_r) is referred to as mean shear or 'rapid' term, and the second part (p_s) is referred to as the turbulent, or 'slow' term. Both are associated with homogeneous Neumann wall boundary condition, and can be determined for a given spatial distribution of fluctuating velocity. The third part (p_{st}) results from solving a Laplace equation with inhomogeneous boundary conditions, and it is referred to as Stokes pressure. This can be determined once the distribution of the wall-normal velocity fluctuations near the wall is given. As noted by Kim (1989), the above triple splitting is not unique, and inhomogeneous boundary conditions can just as well be incorporated with the rapid or the slow term.

The magnitude of the Stokes pressure fluctuations can be inferred by taking the Fourier transform of (B3) in the homogeneous directions, yielding

$$\frac{1}{\rho} \left. \frac{\mathrm{d}\hat{p}_{st}}{\mathrm{d}y} \right|_{y=0} = \nu \left. \frac{\mathrm{d}^2 \hat{v}}{\mathrm{d}y^2} \right|_{y=0}, \tag{B4}$$

where $\hat{p}_{st}(y)$ and $\hat{v}(y)$ represent the Stokes pressure and wall-normal velocity in Fourier space. The pressure fluctuations associated with each Fourier mode can be determined as

$$\hat{p}_{st}(k_x, y, k_z) = -\frac{\rho \nu}{\tilde{k}} \left. \frac{\mathrm{d}^2 \hat{v}}{\mathrm{d}y^2} \right|_{y=0} e^{-\tilde{k}y}, \tag{B5}$$

1010 A10-19

where $\tilde{k} = (k_x^2 + k_z^2)^{1/2}$ is the effective wavenumber for the given Fourier mode, with k_x and k_z the wavenumbers in the streamwise and spanwise directions, respectively. An approximate prediction for the magnitude of the Stokes pressure fluctuations can be obtained by inspecting the two-dimensional spectral maps of v near the wall (see figure 12*a*). These maps reveal a single dominant energetic site corresponding to $\lambda_\theta^+ \approx 41.1$, $\lambda_x^+ \approx 144.2$, yielding $\tilde{k}^+ \approx 0.16$. Although the spectrum is shown only for pipe flow case G, it aligns well with findings at much lower Reynolds numbers (Kim *et al.* 1987), suggesting universality across Reynolds-number variations. Analysis of the distribution of wall-normal velocity variance from DNS, as reported in figure 12(*b*), further suggests that

$$\langle v^2 \rangle^+ \overset{y^+ \to 0}{\simeq} C_v (y^+)^4, \tag{B6}$$

with $C_v \approx 2 \times 10^{-4}$ as a universal constant. From this, and noticing that in the wall proximity

$$\hat{v}(y) \simeq \frac{1}{2} \left. \frac{\mathrm{d}^2 \hat{v}}{\mathrm{d}y^2} \right|_{y=0} y^2, \tag{B7}$$

it follows that

$$\left| \frac{\mathrm{d}^2 \hat{v}}{\mathrm{d}y^2} \right|_{y=0} \approx 2 C_v^{1/2}. \tag{B8}$$

Finally, (B5) yields

$$p_{rms}^+(y^+) \approx \frac{2 C_v^{1/2}}{\tilde{k}^+} \mathrm{e}^{-\tilde{k}^+ y^+}. \tag{B9}$$

This solution demonstrates that the inner-scaled intensity of the Stokes pressure fluctuations is independent of the Reynolds number, with a wall value of $p_{rms}^+|_{y=0} \approx 0.177$, hence much smaller than the overall pressure root mean square (r.m.s.) value (see figure 4). Furthermore, (B9) conveys that the Stokes pressure fluctuations decay exponentially with the wall distance and become negligible outside the viscous sublayer. This prediction aligns closely with the numerically computed distributions of the r.m.s. Stokes pressure extracted from channel flow DNS data (Kim 1989).

For many practical purposes, one could then use the homogeneous boundary condition for both the rapid and slow pressure components, effectively ignoring the Stokes pressure when considering the r.m.s. fluctuations. However, it is important to note that this does not imply the wall has no effect on the pressure fluctuations. Rather, it suggests that most of the wall's influence is already accounted for in the source terms, which are modified by the no-slip boundary conditions on the velocities. Therefore, the explicit influence of the wall through the boundary condition in the Poisson equation is minimal.

REFERENCES

AHN, B.K., GRAHAM, W.R. & RIZZI, S.A. 2010 A structure-based model for turbulent-boundary-layer wall pressures. *J. Fluid Mech.* **650**, 443–478.

BLAKE, W.K. 2017 *Mechanics of Flow-Induced Sound and Vibration, Volume 2: Complex Flow-Structure Interactions*. Academic Press.

BRADSHAW, P. 1967 'Inactive' motion and pressure fluctuations in turbulent boundary layers. *J. Fluid Mech.* **30**, 241–258.

CHEN, X. & SREENIVASAN, K.R. 2022 Law of bounded dissipation and its consequences in turbulent wall flows. *J. Fluid Mech.* **933**, A20.

DENNIS, D.J.C. & SOGARO, F.M. 2014 Distinct organizational states of fully developed turbulent pipe flow. *Phys. Rev. Lett.* **113** (23), 234501.

FARABEE, T.M. & CASARELLA, M.J. 1991 Spectral features of wall pressure fluctuations beneath turbulent boundary layers. *Phys. Fluids* **3**, 2410–2420.

GRESHO, P.M. & SANI, R.L. 1987 On pressure boundary conditions for the incompressible Navier–Stokes equations. *Intl J. Numer. Meth. Fluids* **7** (10), 1111–1145.

HELLSTRÖM, L.H.O. & SMITS, A.J. 2014 The energetic motions in turbulent pipe flow. *Phys. Fluids* **26** (12), 125102.

HOYAS, S. & JIMÉNEZ, J. 2006 Scaling of velocity fluctuations in turbulent channels up to $Re_\tau = 2003$. *Phys. Fluids* **18**, 011702.

HU, Z.W., MORFEY, C.L. & SANDHAM, N.D. 2006 Wall pressure and shear stress spectra from direct simulations of channel flow. *AIAA J.* **44** (7), 1541–1549.

HWANG, Y. 2015 Statistical structure of self-sustaining attached eddies in turbulent channel flow. *J. Fluid Mech.* **767**, 254–289.

HWANG, Y. 2024 Near-wall turbulence intensity as $Re \rightarrow \infty$. *Phys. Rev. Fluids* **9**, 044601.

JIMÉNEZ, J. & HOYAS, S. 2008 Turbulent fluctuations above the buffer layer of wall-bounded flows. *J. Fluid Mech.* **611**, 215–236.

KIM, J. 1989 On the structure of pressure fluctuations in simulated turbulent channel flow. *J. Fluid Mech.* **205**, 421–451.

KIM, J. & MOIN, P. 1985 Application of a fractional-step method to incompressible Navier–Stokes equations. *J. Comput. Phys.* **59** (2), 308–323.

KIM, J., MOIN, P. & MOSER, R.D. 1987 Turbulence statistics in fully developed channel flow at low Reynolds number. *J. Fluid Mech.* **177**, 133–166.

KIM, K.C. & ADRIAN, R.J. 1999 Very large-scale motion in the outer layer. *Phys. Fluids* **11** (2), 417–422.

MANSOUR, N.N., KIM, J. & MOIN, P. 1988 Reynolds-stress and dissipation-rate budgets in a turbulent channel flow. *J. Fluid Mech.* **194**, 15–44.

MARUSIC, I. & MONTY, J.P. 2019 Attached Eddy model of wall turbulence. *Annu. Rev. Fluid Mech.* **51** (1), 49–74.

MEHREZ, A., PHILIP, J., YAMAMOTO, Y. & TSUJI, Y. 2019 Pressure and spanwise velocity fluctuations in turbulent channel flows: logarithmic behavior of moments and coherent structures. *Phys. Rev. Fluids* **4** (4), 044601.

MONKEWITZ, P.A. 2022 Asymptotics of streamwise Reynolds stress in wall turbulence. *J. Fluid Mech.* **931**, A18.

ORLANDI, P. 2000 *Fluid Flow Phenomena: A Numerical Toolkit*. Kluwer.

PANTON, R.L., LEE, M. & MOSER, R.D. 2017 Correlation of pressure fluctuations in turbulent wall layers. *Phys. Rev. Fluids* **2** (9), 094604.

PERRY, A.E. & ABELL, C.J. 1977 Asymptotic similarity of turbulence structures in smooth-and rough-walled pipes. *J. Fluid Mech.* **79** (04), 785–799.

PERRY, A.E. & CHONG, M.S. 1982 On the mechanism of wall turbulence. *J. Fluid Mech.* **119**, 173–217.

PIROZZOLI, S. 2024 On the streamwise velocity variance in the near-wall region of turbulent flows. *J. Fluid Mech.* **989**, A5.

RUSSO, S. & LUCHINI, P. 2017 A fast algorithm for the estimation of statistical error in DNS (or experimental) time averages. *J. Comput. Phys.* **347**, 328–340.

SILLERO, J.A., JIMÉNEZ, J. & MOSER, R.D. 2013 One-point statistics for turbulent wall-bounded flows at Reynolds numbers up to $\delta^+ \simeq 2000$. *Phys. Fluids* **25**, 105102.

TOWNSEND, A.A. 1961 Equilibrium layers and wall turbulence. *J. Fluid Mech.* **11** (1), 97–120.

TOWNSEND, A.A. 1976 *The Structure of Turbulent Shear Flow*. 2nd edn. Cambridge University Press.

TSUJI, Y., FRANSSON, J.H.M., ALFREDSSON, P.H. & JOHANSSON, A.V. 2007 Pressure statistics and their scaling in high-Reynolds-number turbulent boundary layers. *J. Fluid Mech.* **585**, 1–40.

VERZICCO, R. & ORLANDI, P. 1996 A finite-difference scheme for three-dimensional incompressible flows in cylindrical coordinates. *J. Comput. Phys.* **123** (2), 402–414.

WILLMARTH, W.W. 1975 Pressure fluctuations beneath turbulent boundary layers. *Annu. Rev. Fluid Mech.* **7** (1), 13–36.

XU, H.H.A., TOWNE, A., YANG, X.I.A. & MARUSIC, I. 2020 Pressure power spectrum in high-Reynolds number wall-bounded flows. *Intl J. Heat Fluid Flow* **84**, 108620.

YU, M., CECI, A. & PIROZZOLI, S. 2022 Reynolds number effects and outer similarity of pressure fluctuations in turbulent pipe flow. *Intl J. Heat Fluid Flow* **96**, 108998.